


Warps and Breaks in Circumbinary Discs

Ian Rabago^{1,2} , Zhaohuan Zhu^{1,2} , Stephen Lubow³ , and Rebecca G. Martin^{1,2} 

¹Department of Physics and Astronomy, University of Nevada, Las Vegas 4505 S. Maryland Parkway Las Vegas, NV 89154, USA

²Nevada Center for Astrophysics, University of Nevada, Las Vegas 4505 S. Maryland Parkway Las Vegas, NV 89154, USA

³Space Telescope Science Institute, Baltimore, MD 21218

Accepted XXX. Received YYY; in original form ZZZ

ABSTRACT

Disc warping, and possibly disc breaking, has been observed in protoplanetary discs around both single and multiple stars. Large disc warps can break the disc, producing observational signatures in kinematics and shadowing along the outer disc. In this work, we use comparisons of disc timescales to derive updated formulae for disc breaking, with better predictions as to when and where a disc is expected to break and how many breaks could occur. Disc breaking is more likely for discs with small inner cavities, cooler temperatures, and steeper power-law profiles. Thus, thin, polar-aligned discs are more likely to break. We test our analytic formulae using 3D grid-based simulations of protoplanetary discs warped by the gravitational torque of an inner binary. We reproduce the expected warp behaviors in different viscosity regimes and observe disc breaking at locations in agreement with our derived equations. As disc breaking is observed only for discs with low viscosity, we also consider a viscous criterion for disc breaking, where rapid alignment to the precession vector can prevent a break by reducing the maximum misalignment between neighboring rings. We apply these results to the GW Orionis circumtriple disc, and find that the precession induced from the central stars can break the disc if the disc is relatively thin. We expect repeated or multiple disc breaking to occur for discs with sufficiently steep power law profiles. We simulate a disc with steep power-law profiles, and observe two separate breaking events at locations in rough agreement with our analytical predictions.

Key words: accretion, accretion discs – protoplanetary discs – hydrodynamics – methods: numerical – binaries:general – stars:individual:GW Orionis

1 INTRODUCTION

Many astrophysical discs are observed to not lie entirely within a single plane. These discs are generally referred to as “warped” discs, changing their orientation in three-dimensional space with radius. Warped discs have been found at all different astrophysical scales through direct observation, from planetary rings to the discs of galaxies (Burke 1957; Kerr et al. 1957; Shu et al. 1983; Burrows et al. 1995). Many other warps have been inferred from their effects on their nearby surroundings, including maser emission in the vicinity of supermassive black holes (Miyoshi et al. 1995; Martin 2008), to explain long-term periodicity in close X-ray binaries (Katz 1973; Petterson et al. 1991; Scott et al. 2000), and shadows cast in protoplanetary discs (Marino et al. 2015; Debes et al. 2017). The ubiquity of such a structure warrants careful study of its behavior and evolution.

The warping of discs is a well-studied phenomenon, and a large amount of work has gone into deriving the analytic behavior of the evolution and testing this behavior via numerical methods (see Papaloizou & Pringle 1983; Pringle 1992; Papaloizou & Lin 1995; Ogilvie 1999; Lodato & Pringle 2007; Lodato & Price 2010, as well as Nixon & King 2016 for an overall review). In a warped disc, the angular momentum vector of the disc \mathbf{L} changes with radius, r . The overall evolution of a warped disc can be effectively described with two different behaviors, depending on the relative sizes of the disc aspect ratio of scale height to radius, h/r , to its α -viscosity coefficient

(Shakura & Sunyaev 1973). Thin, high-viscosity discs with $\alpha > h/r$ are said to be in the *diffusive* or *viscous* regime, where the warp flattens diffusively on timescales inversely proportional to a second viscosity coefficient ν_2 . Thicker, low viscosity discs with $\alpha < h/r$, are instead considered to be in the *bending wave* or *wave-like* regime, in which the warp launches a wave which propagates through the disc.

In the diffusive regime, the evolution of a warped disc may be described as a diffusion equation in \mathbf{L} with terms proportional to the standard viscosity ν_1 and a warp viscosity ν_2 . Terms including ν_1 describe the standard evolution of a flat disc (i.e. Lynden-Bell & Pringle 1974), while terms including ν_2 describe the evolution of the warp in the disc (Pringle 1992). There are also additional terms present including a third viscosity term ν_3 , which describe an induced precession from the warp as neighboring annuli induce a torque perpendicular to the direction of the warp (Ogilvie 1999). Subsequent works have also derived evolution equations in the bending wave regime in which the effects of pressure dominate over viscosity (Papaloizou & Lin 1995; Demianski & Ivanov 1997; Lubow & Ogilvie 2000), as well as more general sets of equations that encompass both regimes (Martin et al. 2019; Dullemond et al. 2022).

The relative sizes of the viscosity coefficients ν_1 , ν_2 , and ν_3 also depend on the warp amplitude, characterized by the dimensionless parameter ψ which is defined as

$$\psi = r \left| \frac{\partial \mathbf{I}(r)}{\partial r} \right|. \quad (1)$$

The dependence of the coefficients on ψ for large, non-linear warps and the disc viscosity α is characterized in [Ogilvie \(1999\)](#).

When warps become very large, the disc may be unable to communicate across the warp effectively. The warp may become unstable, and disc breaking can occur, splitting the disc into separate rings. This phenomenon has been studied analytically ([Doğan et al. 2018](#); [Raj et al. 2021](#)), and previously observed in simulations of discs around single and binary black holes ([Nixon et al. 2012, 2013](#); [Nealon et al. 2015](#)). Disc breaking is also thought to have occurred in some discs as a possible explanation for the observed geometry or accretion kinematics ([Casassus et al. 2015](#); [Facchini et al. 2018](#); [Zhu 2019](#); [Kraus et al. 2020](#); [Nealon et al. 2022](#)). However, the exact conditions that lead a disc to break are still unclear, as well as where the location of the break (known as the breaking radius) will occur.

In this paper, we attempt to improve the current known methods of determining a disc breaking event by studying the evolution of a disc under the influence of an external precession torque. In our context, we consider a misaligned disc around a binary star system, analogous to protoplanetary discs forming in young star clusters. We will see that under the influence of the binary, the disc can develop warps and breaks depending on the internal conditions of the disc.

The previous studies of disc breaking in binaries have been largely based on the use of the SPH code. With this Lagrangian code the resolution is determined by the particle density and is therefore a concern near disc breaks. In this paper we apply an Eulerian code whose resolution is instead limited by the grid size. In addition, we take advantage of the fact that disc breaking occurs more easily for circumbinary discs that are evolving to a polar orientation, compared to evolving to a coplanar orientation, around eccentric orbit binaries.

Our paper is organized as follows. In [Section 2](#), we discuss the timescales relevant to disc breaking and describe our new method of calculating the location of a break. [Section 3](#) outlines the numerical methods we use to test our new method for calculating the breaking radius. We present our results in [Section 4](#). We discuss these results in [Section 5](#), and conclude in [Section 6](#).

2 TIMESCALES OF DISC EVOLUTION

In this section, we examine the different evolutionary timescales that affect a warped disc, and consider how these timescales determine the breaking radius of the disc. We consider the situation of a circumbinary disc surrounding a central binary. The binary consists of two stars with masses M_1 and M_2 , with total mass labeled $M_{\text{tot}} = M_1 + M_2$, orbital semi-major axis a_b , and orbital eccentricity e_b . We choose radial power-law profiles for midplane density, temperature, and surface density, using the indices d , s , and p given by ¹

$$\rho(r) = \rho_0 \left(\frac{r}{r_0} \right)^{-d}, \quad (2)$$

$$T(r) = T_0 \left(\frac{r}{r_0} \right)^{-s} \quad (3)$$

¹ Previous works commonly use p for the midplane density index and q for either the temperature or sound speed index. There is also some inconsistency when considering the sign of the index, i.e. if the negative sign of the exponent is included in the variable (e.g. [Takeuchi & Lin \(2002\)](#)). We choose positive indices and our variable names to remain consistent with the variables in [Lubow & Martin \(2018\)](#), and to avoid confusion with the variable used for the binary mass ratio.

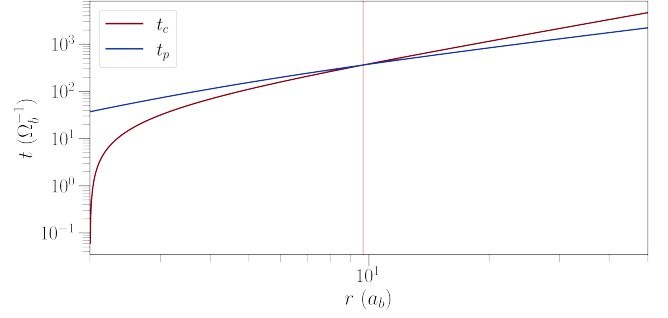


Figure 1. Disc timescales t_p and t_c as a function of disc radius on a logarithmic scale. The red vertical line indicates the expected location of a disc breaking event based on Equations (12) and (13). For this figure, we consider a nearly coplanar disc around an equal mass binary with $e_b = 0.5$, extending from $r_{\text{in}} = 2a_b$ to $r_{\text{out}} = 50a_b$. The disc has a constant scale height $h/r = 0.1$, with power law slopes of $p = 1.5$ and $s = 1.0$.

and

$$\Sigma(r) = \Sigma_0 \left(\frac{r}{r_0} \right)^{-p}. \quad (4)$$

For a steady state Keplerian disc, these power-law indices are related through the equation

$$2d + s - 2p = 3 \quad (5)$$

since $\rho = \Sigma/H$ (e.g. [Pringle 1981](#)) and the sound speed is given by $c_s = h\Omega \propto T^{1/2}$.

2.1 Disc breaking in the wave-like regime

The torque from the binary potential causes a ring of material to nodally precess at a frequency

$$\omega_p(r) = k \left(\frac{a_b}{r} \right)^{7/2} \Omega_b \quad (6)$$

(e.g. [Farago & Laskar 2010](#)), where Ω_b is the orbital frequency of the binary, r is the radius of the ring, and k is a constant which depends on the binary masses, eccentricity, and whether the disc is close to a coplanar or polar configuration ([Martin & Lubow 2017](#); [Zanazzi & Lai 2018](#); [Lubow & Martin 2018](#); [Martin & Lubow 2018](#)). For a circumbinary disc, the inner regions feel a stronger torque from the binary than the outer regions. In the absence of communication between the rings of the disc, the inner rings precess faster than the outer rings. Therefore depending upon the communication timescale between the rings of the disc, the disc may become warped.

If the radial communication timescale is short compared with the precession timescale then the disc can precess like a solid body. For a disc with inner radius r_{in} and outer radius r_{out} , the global precession timescale t_p of the disc as a solid body is given by

$$t_p = \frac{2(1+p)r_{\text{in}}^{1+p}r_{\text{out}}^{5/2-p}}{|k|(5-2p)a_b^{7/2}\Omega_b}. \quad (7)$$

The radial communication timescale in the wave-like regime t_c is given by

$$t_c = \frac{4}{(2+s)\Omega_b h_{\text{out}}} \left(\frac{r_{\text{out}}}{a_b} \right)^{3/2} \quad (8)$$

where h_{out} is the scale height at the outer edge of the disc.

We expect disc breaking to occur when the global precession timescale is shorter than the communication timescale, $t_p < t_c$. Analytic estimates of the disc breaking radius have been given in many previous works (e.g. Nixon et al. 2013; Lubow & Martin 2018). Combining Equations (7) and (8) and solving for r_{out} as the breaking radius gives

$$r_{\text{break}} = \left[\frac{(p+1)(s+2)h_{\text{out}}}{2(5-2p)|k|} \left(\frac{r_{\text{in}}}{a_b} \right)^{p+1} \right]^{\frac{1}{p-1}} a_b. \quad (9)$$

The timescales given in Equations (7) and (8) assume that $r_{\text{in}} \ll r_{\text{out}}$, i.e. that the discs have a large radial extent. During breaking events, newly created discs may break off as radially thin rings, so a more complete description of these equations is required.

Here we attempt to derive a more refined estimate of t_p and t_c by revisiting these equations. The disc nodal precession frequency is given in Equations (16)-(17) of Lubow & Martin (2018) as

$$\omega_p = k \frac{\int_{r_{\text{in}}}^{r_{\text{out}}} \Sigma r^3 \Omega (a_b/r)^{7/2} dr}{\int_{r_{\text{in}}}^{r_{\text{out}}} \Sigma r^3 \Omega dr} \Omega_b \quad (10)$$

where Ω is the orbital frequency and k is a general constant depending on the parameters of the binary. Equation (16) of Lubow & Martin (2018) and Equation (5) of Smallwood et al. (2019) give the value of k as

$$k = \begin{cases} -\frac{3}{4} \sqrt{1 + 3e_b^2} - 4e_b^4 \frac{M_1 M_2}{M_{\text{tot}}^2} & \text{for a nearly coplanar disc,} \\ \frac{3}{4} \sqrt{5} e_b \sqrt{1 + 4e_b^2} \frac{M_1 M_2}{M_{\text{tot}}^2} & \text{for a nearly polar disc.} \end{cases} \quad (11)$$

The fraction containing the binary masses $M_1 M_2 / M_{\text{tot}}^2$ may also be written as $q/(1+q)^2$, where $q = M_2/M_1$ is the binary mass ratio. Equation (11) implies that the value of k is largest (and thus the precession rate quickest) for equal mass binaries. Low eccentricity binaries produce larger k values for coplanar discs, while higher eccentricity binaries are better for polar discs.

We define the disc precession time to be $t_p = 1/\omega_p$. Evaluating the integrals in Equation (10) for a disc with the surface density profile in Equation (4) and Keplerian rotation profile $\Omega = \Omega_K \propto r^{-3/2}$, we find for the disc precession time

$$t_p = \frac{-2(1+p)}{k(5-2p)\Omega_b} \left(\frac{r_{\text{in}}}{a_b} \right)^{7/2} \left[\frac{(r_{\text{out}}/r_{\text{in}})^{5/2-p} - 1}{(r_{\text{out}}/r_{\text{in}})^{-(1+p)} - 1} \right]. \quad (12)$$

In the limit that $r_{\text{out}} \gg r_{\text{in}}$, this tends to Equation (7).

To calculate the communication time of a warp across the disc, we consider the travel speed of bending waves starting from the inner edge. These waves travel at half the local sound speed (Papaloizou & Lin 1995). Assuming a radial power-law profile for the disc temperature as in Equation (3), we calculate the radial communication time as

$$t_c = \int_{r_{\text{in}}}^{r_{\text{out}}} \frac{2}{c_s(r)} dr = \frac{4}{s+2} \left[r_{\text{out}}^{s/2+1} - r_{\text{in}}^{s/2+1} \right]. \quad (13)$$

An example of these timescales are shown as a function of disc radius in Figure 1. For geometrically thin rings ($r_{\text{in}} \approx r_{\text{out}}$), Equations (12) and (13) reproduce the correct limiting behavior ($t_p \approx 1/\omega_p$ and $t_c \approx 0$), which Equations (7) and (8) do not.

Using Equations (12) and (13), we can derive an updated location for the breaking radius. In regions where $t_p > t_c$, a precession induced warp can be communicated via bending waves and allow the disc to precess rigidly. Taking the breaking radius r_{break} to be the value of r_{out} for which $t_p = t_c$; for $r_{\text{out}} > r_{\text{break}}$ we have that $t_p < t_c$ and the disc will precess faster than it is able to communicate the

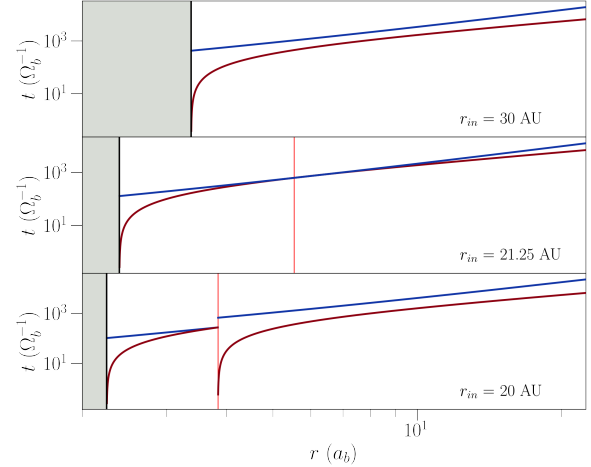


Figure 2. Predicted disc evolution of the Kraus et al. (2020) parameters, as inferred from our timescale equations. In each panel the lines are the same as Fig. 1. The shaded region indicates the inner cavity of the disc. *Top:* Early on, the inner edge of the disc is far enough out that a break does not occur. *Middle:* As the disc evolves, the inner edge drifts inwards until $r_{\text{in}} = 21.25$ au, where a break spontaneously occurs in the disc at 49 au. *Bottom:* As the inner edge continues to drift inwards, so does the expected breaking radius. Once the inner disc reaches an inner radius of 20 au, the expected breaking radius has moved to a radius of roughly 35 au.

precession to its outer edge, causing the disc to break. This criterion approximately says that the breaking radius occurs at the distance that a bending wave can travel over a disc precession timescale, starting from the disc inner edge.

Whether the curves of t_p and t_c intersect is determined by the disc geometry ($r_{\text{in}}, r_{\text{out}}, h/r$), disc structure (power-law slopes d, s , and p), and inner binary arrangement (q, a_b , and e_b , which determine the constant k). The slope of Equation (12) is determined by the surface density power-law slope p and the ratio $r_{\text{out}}/r_{\text{in}}$, whereas the slope of Equation (13) is determined by the temperature power-law slope s . The location of the inner radius, r_{in} , sets the fastest precession rate of the entire disc and the initial height of the t_p curve, and is a strong factor in determining whether or not a disc will break. Because of this sensitive dependence on r_{in} , nearly polar aligned discs are more likely to have breaks (Section 3.1 and 3.2), since they are able to maintain smaller inner cavities (Franchini et al. 2019) and therefore faster precession rates. In addition, for fixed binary and disc parameters, the precession rate normalized by binary frequency of a nearly polar disc is faster than for a nearly coplanar disc for binary eccentricity $e_b > 0.41$, as follows from Equation (11).

Once the disc breaks into separate rings, the outer disc will have its timescales reset as its inner radius has now moved to the location of the break. These timescales can grow again starting from the inner edge of the outer disc and, depending on the conditions of the outer disc, they may intersect again and cause the outer disc to break into yet another set of rings. Thus, being applied repeatedly, our breaking condition could predict the breaking radii of multiple breaks. In Section 2.4, we explore the possibility of multiple disc breaking in more detail, examining which disc parameters are required to cause multiple disc breaking.

2.2 A Criterion for Viscous Disc Breaking

Discs align towards their precession vector (\mathbf{L}_b for coplanar orientations, or \mathbf{e}_b for polar orientations) in both the wave-like and viscous regimes on a timescale that is roughly inversely proportional to α (King et al. (2013), Lubow & Martin 2018, Eq.29)

$$t_{\text{align}} = \frac{(h/r)^2 \Omega_b}{\alpha (\omega_p)^2}. \quad (14)$$

If the disc aligns significantly faster than the precession rate, the disc will become coplanar to the precession vector before it can precess a significant amount. This can suppress large warps generated by azimuthal “twisting” motions (Raj et al. 2021), which may prevent disc breaking even if the other disc parameters would normally allow for a break to occur. We can express this relation by finding the ratio of t_p to t_{align}

$$\tau(r) = \frac{t_{\text{align}}}{t_p} = \frac{(h/r)^2}{\alpha} t_p \Omega_b. \quad (15)$$

When this ratio is less than 1, $t_{\text{align}} < t_p$ and alignment occurs before disc precession, preventing disc breaking. This criterion is primarily applicable to discs in the diffusive regime, although the factor of $(h/r)^2/\alpha$ suggests it may apply to some discs in the wave-like regime as well. Equation (15) is a simple estimate which only considers the disc scale height at one particular radius; other approaches may take into account how the scale height changes radially across the disc. Various disc breaking criteria have been suggested in the past. Equation (13) of King et al. (2013) considers $t_{\nu_2} \omega_p < 1$ as the criterion to prevent large disc warping in the viscous regime, where t_{ν_2} is the viscous timescale associated with the ν_2 viscosity. We note that in the linear regime of small warps, this criterion and the Equation (15) give opposite stability results because $(\omega_p t_{\text{align}})^{-1} \sim \omega_p t_{\nu_2}$. A short (long) alignment timescale occurs with a long (short) warp viscous timescale. But the ν_2 value for small warps may not apply for cases of disc breaking.

2.3 An Application to GW Orionis

GW Orionis is a hierarchical triple star system surrounded by a large protoplanetary disc (Mathieu et al. 1991; Berger et al. 2011). Resolved images of the system (Bi et al. 2020; Kraus et al. 2020) show a series of dust rings in differing orientations around the central star system as well as distorted velocity maps in ^{12}CO , suggesting that the disc is warped. Observations indicate that the outer disc is inclined with respect to the outer binary orbital plane at an angle of roughly $i = 38^\circ$.

The GW Orionis system has been simulated in previous works, but simulations have shown differing results as to whether the disc will break solely under the influence of the inner star system. In their observational paper, Kraus et al. (2020) use SPH simulations to explain the warped geometry of the system. They simulate the GW Ori disc with an initial radial range of 40 to 200 au, using power-law slopes of $p = 0.2$ and $s = 1.0$ and a very thin disc with $h/r = 0.02$. The disc expands inwards until the inner radius reaches about 30au, where a thin ring breaks off from the inner edge of the disc and precesses independently, eventually aligning with the binary plane. Kraus et al. (2020) interpret this inner ring as a potential origin of the R3 dust ring seen in observations.

Bi et al. (2020) and Smallwood et al. (2021) ran a similar suite of SPH simulations for the GW Ori system, using a disc with the same initial inner edge but a slightly thicker aspect ratio of $h/r = 0.05$ and

power-law slopes of $p = 1.5$ and $s = 1.0$. Their simulations find a disc that warps strongly but does not break through disc precession alone. They suggest that a giant planet embedded in the disc is required to carve a gap first in order for an inner ring to break off. However, they find that a disc with a smaller inner radius, $r_{\text{in}} = 20\text{au}$, can spontaneously generate a break, with a breaking radius of roughly 75 au. From this, they determine that the geometry of the disc is an important factor in determining if a disc is able to break.

Using Equations (12) and (13), it is possible to explain the appearances of both SPH simulations. To model this triple star system with our analytic equations, we assume that the triple star orbit can be approximated by the outer binary orbit of the triple. This assumption is justified for a low binary eccentricity (e.g. Lepp et al. 2023). The binary is composed of $M_1 = 0.742M_{\text{tot}}$ and $M_2 = 0.258M_{\text{tot}}$ with an eccentricity of $e_b = 0.379$. The effect of the inner binary is that it causes apsidal precession of the outer binary (Lepp et al. 2023), but we do not consider this effect when considering the precession of the disc.

For the Kraus et al. (2020) simulation, the initial conditions have $t_p > t_c$ everywhere, indicating a disc with no breaks. However, the two curves approach as the inner edge of the disc drifts inward. Once the inner edge of the disc reaches about 21au, the two curves intersect and a break spontaneously appears at $r_{\text{break}} = 49\text{au}$, producing a thin secondary ring along the inner edge. By the time the inner radius has decreased to 20au, the breaking radius has also moved inwards to a distance of $r_{\text{break}} = 35\text{au}$, a distance that is consistent with the observed location of the ring seen in the SPH simulations. Figure 2 shows the evolution of t_p and t_c in the Kraus disc model. If spontaneous disc breaking occurs in this manner, the material in the inner ring can be shuttled inward into a tight ring similar to what is seen in the GW Ori observations.

The discs used by Bi et al. (2020) and Smallwood et al. (2021) are thicker and have a higher disc temperature, creating smaller values for t_c . This prevents the timescale curves from intersecting unless the inner radius is driven to very small values. Additionally, the change in the shape of the curves causes the value of r_{break} to start from the outer edge of the disc and sweep inwards, instead of starting in the middle like the Kraus et al. (2020) disc. This disc model is unlikely to break using the binary torque alone, and thus a planet-driven explanation is more likely for these disc parameters.

By comparing these simulations, it is clear that the details of the simulation parameters are important in determining the location of a disc break. Observations of the GW Ori system are unable to put strong constraints on the disc parameters, so the GW Ori disc may be able to break under the torque of the binary if it is closer to the Kraus et al. (2020) simulation, i.e. cooler and with lower values of h/r . In Section 3.2, we describe our simulations for the GW Ori system.

2.4 Multiple Disc Breaking

After a disc breaks into two, the inner and outer disc will begin to precess independently. The inner disc is guaranteed to precess rigidly, by the conditions set by the break, but the outer disc may once again precess differentially with its own t_c and t_p starting from the breaking radius which is its new inner edge. If the breaking radius of this new outer disc is within the radial extent of the outer disc, then the outer disc may break again. This process of *multiple disc breaking* can repeat and break the disc into multiple rings for as long as there is disc material, or until the estimates for t_c and t_p above are no longer valid. Some SPH simulations have observed this phenomenon previously, in the context of black hole binaries and the Bardeen-Petterson effect (Nixon et al. 2013; Nealon et al. 2015).

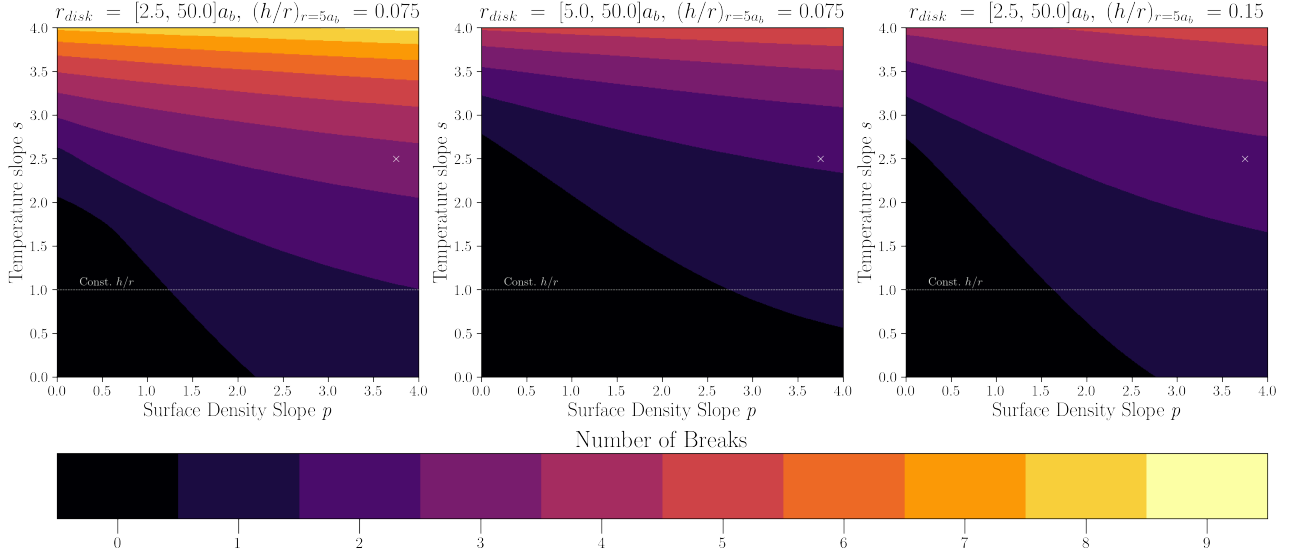


Figure 3. Predicted number of breaks for a disc with a given initial geometry, shown as a function of the surface density and temperature power-law exponents p and s . The radial extent of the disc is given as $r_{\text{disc}} = [r_{\text{in}}, r_{\text{out}}]$ and the initial scale height is given at a distance of $r = 5a_b$. The central binary is an equal mass binary with eccentricity $e_b = 0.5$. *Left:* Initial inner radius and scale height. *Middle:* Effect of a larger inner disc radius. *Right:* Effect of a larger disc aspect ratio. The ‘x’ in each panel marks the disc parameters used in our multiple break simulation (Section 3.3).

To get a better understanding of how the various disc parameters affect the number of disc breaks, in Figure 3 we map out the number of disc breaks for different initial values of r_{in} , r_{out} , and $(h/r)_0$ (the disc geometry) and as a function of the power-law slopes p and s (the disc structure). In this figure, the disc is placed around an equal mass ($M_1 = M_2 = 0.5$), $e_b = 0.5$ central binary. Each panel shows the number of expected disc breaking events for the given initial disc geometry as a function of p and s . In each panel, the horizontal line at $s = 1$ represents discs with a constant h/r throughout; points below this line represent flaring discs, with h/r increasing with radius. In general, discs that are thin, have small inner cavities, and steep profiles are more likely to have multiple breaks.

The effect of changing the inner radius can be seen by comparing the first and second panels. Doubling the inner radius reduces the number of breaks in each region by roughly 1 each. This behavior is consistent with the disc breaking seen in the simulations of [Smallwood et al. \(2021\)](#), who also noticed that disc breaking was dependent on the disc inner radius. Figure 3 also shows that increasing the disc scale height increases the width of each “stripe”, requiring a steeper temperature gradient to achieve multiple breaks.

3 METHODS

We use the grid-based code ATHENA++ ([Stone et al. 2020](#)) to simulate an inclined disc around a central binary. To study the various effects of disc warping and breaking, we run three different sets of simulations, each with slightly different disc and binary setups. Each set is described in the following subsections. Below we describe features common to all of the simulations performed in this paper.

We choose spherical-polar coordinates (r, θ, ϕ) for our simulations. Our simulation domain extends from 5° to 175° in θ , and 0 to 2π in ϕ , and is divided into a grid of 176×384 cells in (θ, ϕ) . We use logarithmically spaced cells in the radial domain. The extent and number of cells in the radial domain r varies depending on the simulation set.

We initialize the density profile of the disc by numerically integrating the density at each grid cell to establish hydrostatic equilibrium according to the power-law profile in Equation (2), and set the vertical profile by numerically integrating the density at each grid cell to establish hydrostatic equilibrium according to the disc scale height $h = c_s / \Omega_K$. Here $r_0 = a_b$, $\rho_0 = 1$ at r_0 , c_s is the local isothermal sound speed $\sqrt{P/\rho}$ at r , and Ω_K is the Keplerian orbital frequency at r . The disc temperature is initialized using the power-law profile in Equation (3), where $T_0 = 1$ at r_0 . We truncate the edges of the disc using an exponential cutoff of the form $\exp[(r - \mu_r)/\sigma_r]$, where μ_r is the location of the disc edge and σ_r the relative scale length of the cutoff. We also use a spherically symmetric density floor with a value of $\rho_{\text{floor}} = 10^{-4}\rho_0$ at $r = 1$ and a power-law slope of d , identical to that of the density profile.

We initialize the disc with an initial scale height of $(h/r)_0$ at $r = r_0$. We use the orbital cooling scheme outlined in Equation (5) of ([Zhu et al. 2015](#)), using a dimensionless cooling time of $t_{\text{cool}} = 0.01\Omega_K^{-1}$. At the simulation boundaries, we set a one-way outflow boundary condition in the radial direction, and reflecting boundary conditions in the polar direction.

The binary components are simulated as gravitational bodies with masses M_1 and M_2 , which orbit with semi-major axis a_b and eccentricity e_b . We integrate the motion of the binary components using a 2nd-order leapfrog integrator, but we do not model the change in the orbits due to interaction with the disc material.

3.1 Polar-Aligning Warped Discs

Our first set of simulations studies the effects of disc warping in a polar-aligning disc around an eccentric binary. As described in Section 2, polar-aligned discs benefit from faster precession times due to smaller central cavities and the response from the central binary, making them ideal for studying disc breaking. Our setup is similar to that used in [Rabago et al. \(2023\)](#), which we review in brief here. The binary components are initialized as equal mass particles ($M_1 = M_2 = 0.5$) with $a_b = 0.28$ and $e_b = 0.5$, placing the binary as

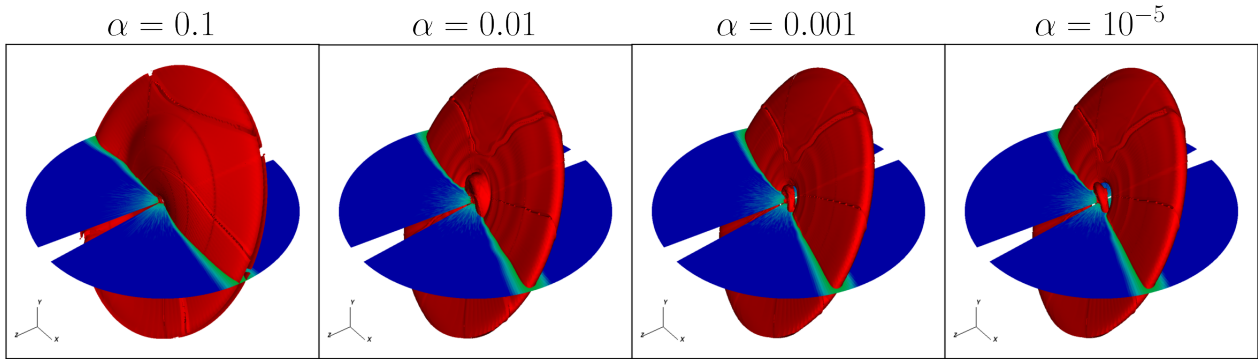


Figure 4. Density contours of the polar-aligning discs at $t = 1000$ binary orbits. Horizontal slice shows disc density, along the plane of the binary. Discs in the $\alpha = 0.01, 0.001,$ and 10^{-5} cases are broken; the inner disc in the $\alpha = 0.01$ simulation has momentarily reconnected with the outer disc as it precesses about the binary eccentricity vector.

close to the inner radial domain as possible. We simulate the region from $0.3 = 1.07a_b$ to $10.0 = 35.7a_b$ using 216 cells in the radial domain. The initial scale height is set at $(h/r)_0 = 0.103$, giving the disc a scale height of $h/r = 0.075$ at $r = 3.5a_b$. We use power-law slopes of $d = 2.25$ and $s = 1.5$ ($p = 1.5$) and truncate the inner edge of the disc using $\mu_r = 2a_b$ and $\sigma_r = 0.35a_b$. The outer edge of the disc extends to the outer radial domain. We vary the α -viscosity parameter between $\alpha = 10^{-1}, 10^{-2}, 10^{-3},$ and 10^{-5} . These values correspond to discs with $h/r < \alpha$ (diffusive regime), $h/r \sim \alpha$ (intermediate case), $h/r > \alpha$ (wave-like regime), and a case for the inviscid limit. We place the binary along the simulation xz -plane and initialize the disc with a 60° inclination to the binary orbital plane. We run these simulations for 1000 binary orbits.

3.2 GW Orionis

We create a suite of simulations that replicates the GW Orionis system. We use the known binary parameters from Kraus et al. (2020), using the AB-C binary separation of $a_b = 8.89$ au as the system scale. Previous simulations of the GW Ori system from Smallwood et al. (2021) found that the motion of the inner AB binary provides smaller effects to the disc compared to the larger motion of the AB-C binary, so we model the GW Ori triple system as a binary to simplify calculations as in Section 2.3. Our binary model consists of the AB binary as one mass $M_{AB} = 0.742M_{\text{tot}}$ and the outer C component as the second mass $M_C = 0.258M_{\text{tot}}$, placed in an orbit with semi-major axis $a_b = 8.89$ au and eccentricity $e_b = 0.379$.

We simulate the region from $1.5a_b$ to $50a_b$, covering a range of roughly 13 au to 450 au. We use 192 cells across the radial domain. The disc is inclined at an angle of 38° relative to the binary. We use power-law exponents of $d = 2.5$ and $s = 1.0$. This gives the disc a surface density profile of $p = 1.5$ and a constant h/r throughout, which we choose to be $(h/r)_0 = 0.075$. We truncate the inner edge of the disc at $\mu_r = 24$ au and use a disc viscosity of $\alpha = 10^{-5}$. We expect this simulation to be similar to the Smallwood et al. (2021) simulation with a small inner radius, generating a break at around $10a_b$. Although the disc viscosity is lower than their simulations, we expect the inner edge of the disc to be truncated at a similar radius due to the torque of the binary and, with $\alpha < h/r$, the disc remains in the wave-like regime and should break in a similar fashion. We run these simulations for 5000 binary orbits, enough time for the inner cavity to settle and the warp to propagate through the disc. We do not

attempt to reproduce the disc from Kraus et al. (2020), due to the thin disc scale height of $h/r = 0.02$ used in their work. Resolving this disc at the required inclination would require a large increase in the overall grid resolution, which we consider prohibitively expensive.

3.3 Multiple Breaks

As described in Section 2.4, the equations for t_p and t_c suggest a disc can undergo multiple breaks if the power-law slope of t_p is less than that of t_c . This can occur given the right combination of disc geometry and density profiles. To examine this possibility, we run an additional simulation with a disc that is predicted to undergo multiple breaks by Equations (7) and (8). To maximize the chance of multiple breaks, we choose a polar-aligning disc with steep density and temperature profiles.

We modify our setup for the polar disc simulations, changing the radial domain so the inner domain remains at $r_{\text{in}} = 1.07a_b$ but extending the outer radial domain to $r_{\text{out}} = 100a_b$ using 272 radial cells across the radial domain. We use power-law profiles of $d = 4.0$ and $s = 2.5$ ($p = 3.75$). We choose the disc scale height to be $(h/r)_{r=5a} = 0.075$. Combined with the temperature profile, the disc a scale height ranges from $(h/r)_{\text{in}} = 0.251$ at the disc inner edge to $(h/r)_{\text{out}} = 0.013$ at $r = 50a_b$. To ensure the disc is resolved as the scale height decreases, we use a single level of mesh refinement to refine the regions between $r = [8.89a_b, 52.1a_b]$ and $\theta = [50.8^\circ, 129.1^\circ]$. The disc viscosity is set to $\alpha = 10^{-5}$, as in the nearly inviscid cases.

A disc with these parameters is predicted to undergo either two or three breaking events, depending on the exact location of the inner radius. The location of this setup is marked on each panel of Figure 3 with an ‘x’. For the left panel, with $r_{\text{in}} = 2.5a_b$, the breaks are predicted to occur at distances of 4.0, 8.6, and 29.1 a_b . We evolve this disc for 1500 binary orbits, enough time for the outer parts of the disc to evolve for a few orbital timescales.

4 RESULTS

4.1 Disc Warping and Breaking

Our polar-aligning simulations exhibit both diffusive and wave-like behavior, depending on our choice of α . Figure 4 shows the various

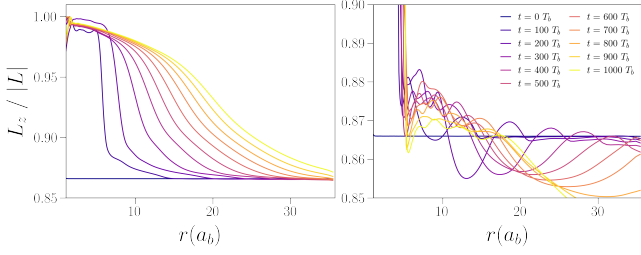


Figure 5. Evolution of the warp profile for the viscous ($\alpha = 0.1$, left) and inviscid cases ($\alpha = 10^{-5}$, right). Each curve represents the z -component of the unit angular momentum vector \mathbf{l}_z as a function of radius. Curves are plotted every 100 binary orbits.

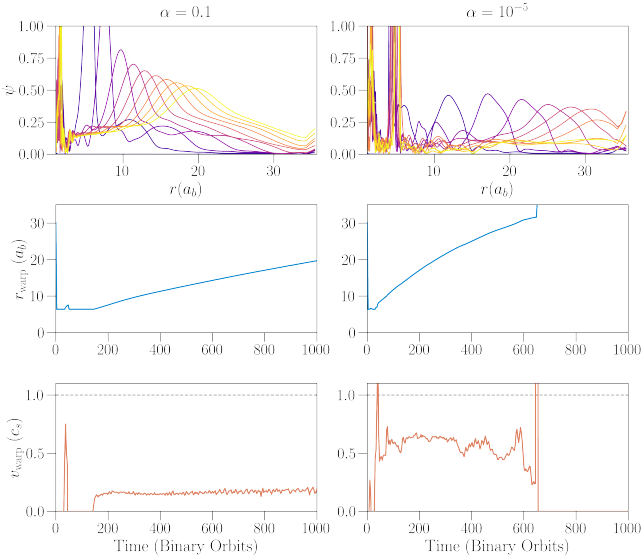


Figure 6. Motion of the warp for the viscous ($\alpha = 0.1$, left) and inviscid cases ($\alpha = 10^{-5}$, right). *Top row:* The ψ parameter plotted against the disc radius. Curves are plotted every 100 binary orbits as in Figure 5. *Middle row:* The radial location of the warp, determined as the local location of maximum ψ . For wave-like propagation, both the initial break and secondary wave propagation are plotted. *Bottom row:* The outward propagation velocity of the warp. The dotted line represents the local sound speed velocity of c_s at the warp radius.

discs at $t = 1000$ binary orbits, displaying varied behaviors in their evolution. For the $\alpha = 10^{-1}$ simulation, the disc develops a strong warp which evolves diffusively, while for the $\alpha = 10^{-2}, 10^{-3}$, and 10^{-5} simulations the disc breaks and exhibits wave-like dispersion. Figure 5 shows the time evolution for both regimes, following the evolution of the z -component of the unit angular momentum vector. In all simulations, an initial warp is excited in the inner disc by the binary precession in the first ~ 200 binary orbits. For the diffusive case, the inner regions of the disc quickly align towards polar due to the short alignment timescale, and the initial warp spreads outwards in the disc diffusively. For the wave-like cases, the initial warp develops into a sharp discontinuity, characteristic of a disc breaking event. After the disc breaks, a smaller disturbance propagates through the outer disc in a wave-like manner.

To determine the location for the warp and follow its movement within the disc, we track the position of maximum ψ as the disc

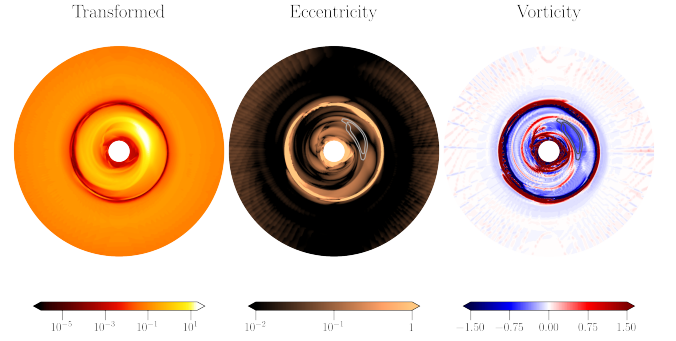


Figure 7. Inner regions of the $\alpha = 10^{-5}$ polar-aligning simulation, projected back onto a single plane. *Left:* Midplane density. The inner disc features an RWI vortex. *Center:* Disc eccentricity. The inner disc is somewhat eccentric. *Right:* Disc vorticity. Note the strong vorticity minimum at the location of the vortex.

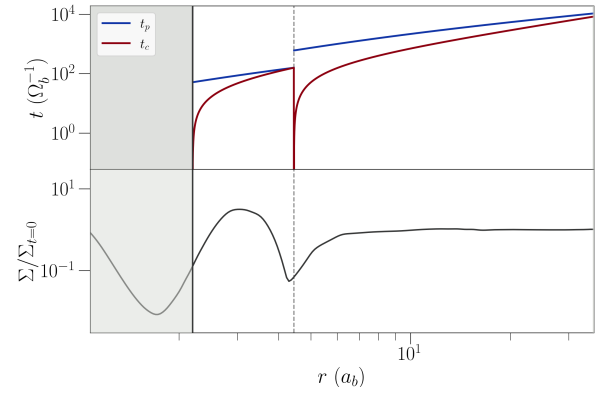


Figure 8. Comparison of the simulated breaking radius to analytical predictions. *Top:* Analytical timescales as predicted from Equations (12) and (13). Here, r_{in} is calculated to be $2.2a_b$ (see text for details). *Bottom:* Surface density of the $\alpha = 10^{-5}$ simulation at $t = 100$ binary orbits, in units of the initial surface density profile Σ_0 . The breaking radius is denoted by the sharp dip in Σ/Σ_0 . In both plots, vertical dashed lines indicate the predicted locations of the breaking radius.

evolves. In the case of a disc that breaks, two peaks in ψ are present, one at the breaking radius and one in the warped outer disc. We find the radial location of both maxima to determine the locations of the disc breaking radius and the warp in the outer disc. The warp location and propagation speed for our warp simulations is shown in Figure 6.

For simulations in the diffusive regime, the inner disc generates a large warp as the disc aligns to the precession axis. The warp creates a large peak in ψ that travels outwards at roughly 0.2 times the local sound speed. Figures 5 and 6 show that the warp starts as a very steep and local feature, but broadens over time, encompassing a range of approximately $10a_b$ by the end of the simulation. A small wave is launched ahead of the main warp (visible in Figure 6 as a series of secondary purple peaks between 10 to $25a_b$, beneath the yellow curves drawn at later times). This wave does not appear with a similar feature in Figure 5. The highly diffusive nature of this disc quickly removes this feature, causing it to disappear by $t = 500t_b$.

Simulations in the wave-like regime show the initial disc breaking at $r_{\text{break}} \sim 4a_b$, independent of the small disc viscosity. After the

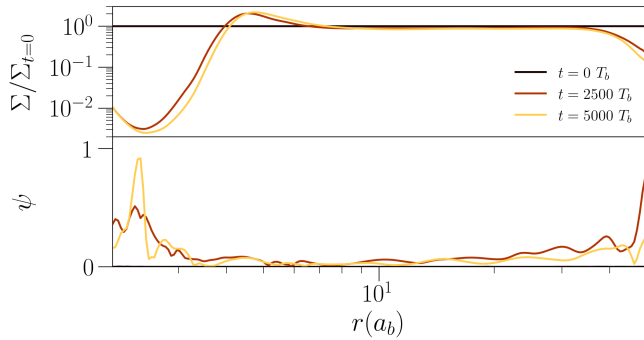


Figure 9. Surface density and warp profile of the GW Ori simulation at $t = 0, 2500, \text{ and } 5000T_b$.

initial breaking event, the breaking radius moves outwards, faster for the intermediate case $\alpha = 0.01$. The bottom panel of Figure 6 shows that the outward warp decreases in velocity as it moves outwards in the disc, the propagation speed following close to one-half of the local sound speed in the disc.

Our analytical equations for disc breaking show close agreement with the location of the break observed in the numerical simulations. In Figure 8 we compare the location of the break in our $\alpha = 10^{-5}$ simulation to the location predicted by Equations (12) and (13). The breaking radius is visible as a sharp drop in the disc surface density. We show the disc surface density at $t = 100$ binary orbits, just after the initial break has formed. Comparing the location of the break at early times is important for accurately determining the location of the breaking radius, since the break slowly drifts outwards in all of our simulations.

To determine the value of r_{in} for our analytic equations, we compare the density-weighted angular momentum of the disc $\int \Sigma r^3 \Omega dr$ to the analytic value expected for a disc with the same surface density power law profile. For this calculation, we choose a snapshot shortly after the initialization, when the disc has had time to equalize but before a break has had time to open up. We consider r_{in} to be the location at which these two values diverge. For the polar-aligning discs, this gives a value of $r_{\text{in}} = 2.2a_b$.

We also observe substructures in the individual discs created after the breaking event. Figure 7 shows the $\alpha = 10^{-5}$ simulation as it would appear “flattened” onto a single plane, as well as the disc eccentricity and vorticity. Simulations with $\alpha = 10^{-3}$ and $\alpha = 10^{-2}$ show similar details in the gap regions, but no substructures in the inner disk. We calculate the disc eccentricity and vorticity in a similar manner to that of Rabago et al. (2023). With low disc viscosities, the inner disc develops a large Rossby Wave Instability (RWI) vortex (Lovell et al. 1999; Li et al. 2000), as well as a localized overdensity and a single-armed spiral. This feature is identical to the vortices seen in the polar discs of Rabago et al. (2023). We observe less features in the outer disc; some faint two-armed spirals are visible at certain times, and no vortices are present. The outer disc has undergone less dynamical times, and so may not have had enough time to develop a large vortex at its inner edge. The gap edge between the inner and outer disc may not be as steep as the edge of the inner disc truncated by the central binary, which may also inhibit the outer disc from forming a strong vortensity minimum and the growth of RWI vortices (Bae et al. 2015).

4.2 GW Orionis

Figure 9 shows the disc surface density and warp strength of the simulation representing the GW Orionis system (Sec.3.2). The disc develops a warp within the first 1000 binary orbits. However, no disc breaking event occurs, even after the next several thousand orbits of the simulation. A light warp persists in the disc throughout the simulation time, but is mostly confined to the inner regions of the disc, and never grows large enough to become unstable and evolve into a full break. We run tests with different α viscosities, simulating out to at least 1000 binary orbits, but none of the simulations are able to create a break in the disc.

The arrangement of the GW Orionis binary changes the strength of the induced precession. The terms in Equation (11) suggest that the precession induced by the binary is strongest for polar discs around high eccentricity, equal mass binaries. The GW Orionis system has a moderate binary eccentricity of $e_b = 0.379$ and a mass ratio, $q = M_C/M_{AB} = 0.348$, making the precession rate normalized by Ω_b of this system about one-fifth as strong as that induced by the polar disks in Section 4.1.

The binary torque truncates the inner edge of the disc at roughly $r_{\text{in}} = 3.5a_b$. This is a larger value of r_{in} than observed in the Smallwood et al. (2021) simulations, and larger than the value we initially used for calculating the breaking radius above. Recalculating the location of the breaking radius with the empirical value of r_{in} changes the disc timescales so that no break occurs in the disc.

4.3 Multiple Breaks

A visualization of our multiple break simulation (Sec. 3.3) is shown in Figure 10. Two disc breaking events are visible, separating the disc into three distinct rings. At the end of the simulation, the disc breaks are located at roughly at radial distances of 7 and $28a_b$, with the outer edge of the disc reaching equilibrium at about $r_{\text{out}} = 60a_b$. The third ring shows a strong warp at roughly $35a_b$. This warp is strong enough for the disc to appear broken due to how thin the disc is at this radius, but subsequent analysis will show that the disc is still communicating across this region. Similar to the polar discs in Section 4.1, we see RWI vortices form in the innermost disc, but not in the second or third discs.

Figure 11 compares the observed locations of each break to the locations predicted by the timescale equations. We find it is difficult to determine a suitable inner radius for this disc. Choosing an inner boundary of $r_{\text{in}} = 2.5a_b$ our analytical equations predict 3 breaks, with the second and third breaks in rough agreement with the locations of the breaks observed in the simulation. The first break, expected at $r = 4.25a_b$, is not observed in the innermost disc. Instead the observed breaks may be roughly fit by choosing $r_{\text{in}} = 4.0a_b$, but this places the “inner edge” of the disc much farther out, in a region where the local surface density is higher than the initial condition.

To better identify the regions in the disc that are communicating, we calculate the azimuthal angle of the shell-averaged angular momentum vector, defined as

$$\phi_L = \arctan\left(\frac{L_y}{L_x}\right), \quad (16)$$

In our multiple break simulation, the z direction is along the binary eccentricity vector and the binary orbit is in the $x - z$ plane, so ϕ_L can be viewed as the longitude of ascending node of the disk in the $x - y$ plane as it circulates around the binary eccentricity vector. Regions of the disc in radial communication will precess together, and thus have roughly the same value of ϕ_L . In Figure 12, we plot

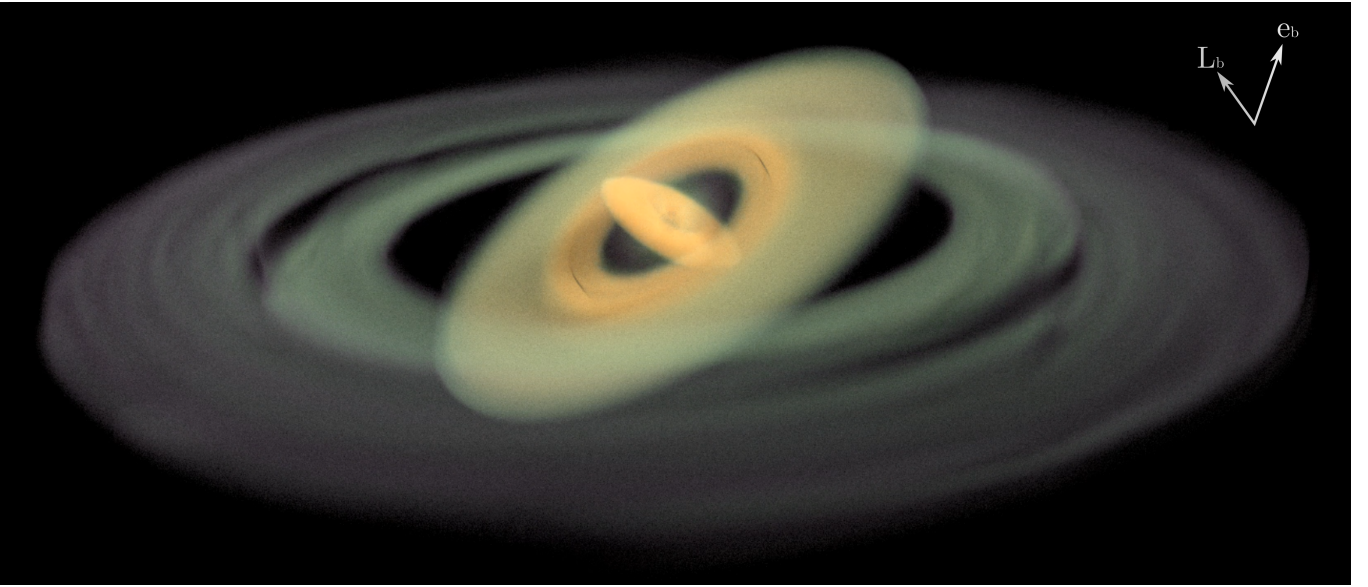


Figure 10. Rendering of the multiple break simulation at $t = 1200$ binary orbits. The directions of \mathbf{L}_b and \mathbf{e}_b are indicated in the top right, with \mathbf{L}_b pointing into the page. The first two breaks at $7a_b$ and $28a_b$ are visible. There is a large warp at $35a_b$ that appears similar to a break, but the disc is not broken at this distance. See text for details. An animation of the disc evolution is also available as an [online video](#).

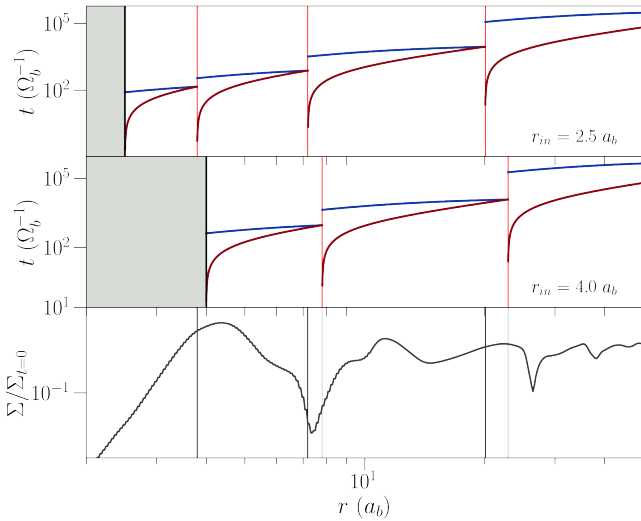


Figure 11. Similar to Figure 8, but for the multiple break simulation. In this figure, each panel shows different choices of the inner radius, $r_{in} = 2.5a_b$ (top) and $r_{in} = 4.0a_b$ (middle). Both choices produce outer breaking locations that are roughly consistent with the observed breaks in the simulation. The bottom panel is from a simulation at a time of $1500 T_b$.

the value of ϕ_L across the disc as a function of simulation time. As the disc evolves and breaks off rings, distinct horizontal bands of color appear, each band corresponding to a separate disc in the final simulation. Disc breaking events are visible as sharp boundaries between two horizontal bands, as the value of \mathbf{L} changes sharply across this region.

In this figure, it can be seen that the innermost disc breaks off almost immediately, in about 100 binary orbits. The outer disc then develops a warp that gradually extends outwards to about $25a_b$, before breaking off a second disc at roughly $1000T_b$. After the disc

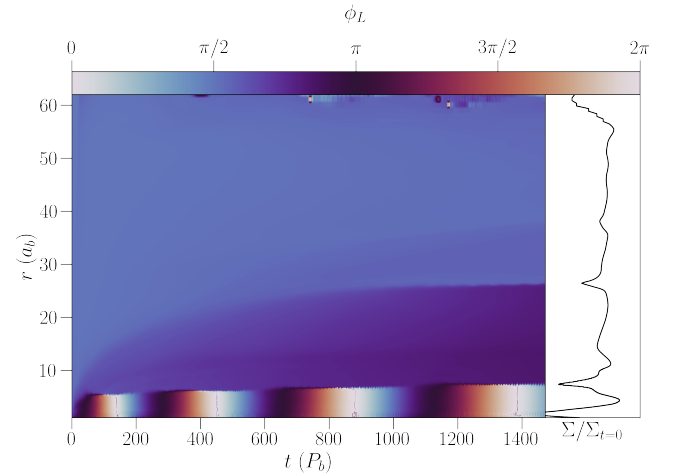


Figure 12. Azimuthal rotation angle plotted as a function of radial location and time. Areas in the same connected disc precess together, and create a band of the same color. By the end of the simulation, three distinct bands are visible, corresponding to the three discs in the simulation. The surface density profile from Figure 11 is also shown at right to compare the locations of the observed gaps. A detailed time evolution of the disc surface density and warp profile is also available as an [online video](#).

breaks at $25a_b$, the warp between the first break and the second break gradually vanishes and this disc region becomes co-planar. This is another indication that the disc loses the communication at the breaking radius and the outer disc cannot torque the inner disc anymore. A faint band can be seen extending from the second disc to about $35a_b$ in the outermost disc, signifying a strong warp. However, since a sharp discontinuity has not yet formed, this band is not yet considered a third breaking event.

The multiple break simulation showcases the difficulty in using

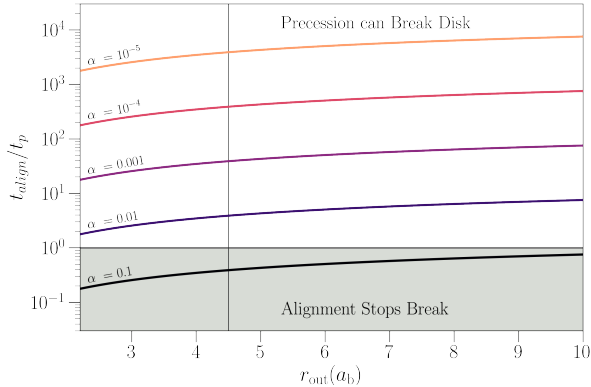


Figure 13. τ as calculated by Equation (15) for different values of α . The vertical line indicates the rough location of the break as seen in our low viscosity simulations.

Equations (12) and (13) to predict the exact location of the breaking radii when multiple breaks are packed together in a small radial range. Breaking events require a few local dynamical timescales to fully develop, so the innermost break will have time to drift outwards while subsequent breaks form and develop. The bottom panel of Figure 11 shows that the surface density, normalized to an initial power-law distribution, is quite disturbed even in regions far away from the breaks, suggesting that the disk no longer follows a power-law distribution even though the analytic equations assume one when calculating the location of a break. We discuss this behavior further in Section 5.1.

5 DISCUSSION

For the polar discs used in Section 3.1, we show the effects of disc viscosity on τ by plotting τ as a function of radius in Figure 13, with the assumption that while calculating t_p all material interior to r is able to precess coherently. We see that for our selected disc parameters, the discs with $\alpha \lesssim 0.01$ maintain $\tau > 1$ for the entirety of the disc and thus are able to break under the induced precession of the binary.

We can estimate ν_2 and ν_3 for our $\alpha = 0.1$ simulation using Figures 4 and 5 of Ogilvie (1999). From our Figure 6, the maximum warp amplitude is roughly $\psi_{\max} = 0.5 - 0.75$, at a distance of $r = 10a_b$. This corresponds to warp viscosities of $\nu_2 = 0.019a_b^2\Omega_b$, $\nu_3 = 0.0013a_b^2\Omega_b$, and $t_{\nu_2} = 5000\Omega_b^{-1}$.

We note that, for the simulations in Section 4.1, there is a change in the overall disc orientation of about 5 to 10 degrees from its initial orientation. This change occurs faster than the local precession timescale induced by the binary, and instead occurs as the warp (diffusive or wave-like) propagates through the disc. This effect is partially visible in Figure 4, since the disc, initialized in alignment with the simulation x -axis, is now misaligned at the end of the simulation. We consider this to be an effect of the ν_3 warp viscosity, which has caused the entire disc to precess.

5.1 Efficacy of the Disc Breaking Equations

The location and number of breaking radii determined by Equations (12) and (13) is a sensitive function of the disc parameters,

particularly the inner disc radius r_{in} . Because of this sensitivity, small adjustments in the value of r_{in} results in large changes in the breaking radius. Conversely, small adjustments in the location of the breaking radii produce relatively minor changes in the required value of r_{in} . Thus, Equations (12) and (13) can easily be made consistent with simulations or observations by finely adjusting the disc parameters to match the observed location(s) of the breaking radius, but it is more difficult to predict the location of emergent breaks starting from the initial disc conditions.

When examining our polar disc simulations in Section 4.1, we initially find the expected breaking radii are different from our initial guess as the inner radius shifts and reaches a quasi-steady state. Once we adjust the value of r_{in} to account for this change, the predicted breaks are in much closer agreement. For the multiple break simulation (Section 4.3), we have a harder time trying to match both the observed breaking locations and the location of the inner radius simultaneously, especially when multiple breaks are packed in a small radial range.

The nature of this sensitivity leads to some difficulty in using Equations (12) and (13) to predict the location of disc breaks. There is no clear location at which the gas at the inner radius of the disc acts as an “edge” and stops precessing as a solid body with the rest of the disc. Thus, different definitions of r_{in} using surface density cutoffs, precession rates, or other methods will calculate slightly different values, which will lead to greatly differing estimates of the breaking radii. Our simulations of GW Ori in Section 4.2 show that the differences in code formulation (SPH vs. grid-based) can also change the location of r_{in} , further complicating this issue. This behavior was also noted in the simulations by Young et al. (2023), who comment that the wide dependence on disc and binary parameters make the creation of a disk breaking equation a challenging matter.

Our analytic equations are also restricted by their lack of full coverage of the possible parameters. Previous SPH simulations have observed a dependence of disc breaking and inclination to the precession vector (Facchini et al. 2013; Nealon et al. 2015), suggesting that disc breaks are more likely for highly inclined or retrograde discs, and may not occur if the mutual inclination between the disc and precession vectors (prograde or retrograde) is small. Analysis by Doğan et al. (2018) and Raj et al. (2021) suggest that a warp may continue to grow unstably if the warp amplitude ψ is beyond a critical limit ψ_c , dependent on the disc viscosity. Our current equations do not include any factors related to these parameters, and so do not capture any related effects when determining a breaking radius. The current analysis is relatively simple and is strictly analytic, using the initial power-law profiles set at the beginning of the simulation to calculate the breaking radius. As the binary-disc system evolves, the gas may settle towards different power-law profiles than those set by the initial conditions, or towards a radial distribution not approximated by a power-law profile, as seen in Figure 11. Future analysis may improve this method by directly integrating the disc radial profiles at later times to provide better calculations of the disc timescales.

5.2 Observational Signatures

The changing orientation of warped discs is known to produce specific observable signatures. Warping changes the projection of the disc onto the sky plane, and produces twisted or S-shaped contours when viewed in molecular lines. This feature has been observed in the GW Orionis circumtriple system (Bi et al. 2020; Kraus et al. 2020) as well as within the cavities of some transition discs such as HD 142527 (Casassus et al. 2015), and can be reproduced using simulations of warped discs (Juhász & Facchini 2017; Smallwood

et al. 2021). High resolution kinematics of warped discs may be able to determine the strength of a disc warp, and may aid in determining if an observed warp is also a break, as well as the flows in the region between the individual discs.

Broken discs have similar observational signatures. If the inner and outer discs are in different orientations, each disc will have differently oriented and possibly separated butterfly patterns in CO channel maps (Zhu 2019). The inner disc will cast shadows as a pair of dark lanes onto the outer disc. The orientation of these lanes may not be symmetric around the disc, and their pattern speed around the disc may not follow the precession rate of the inner disc, depending on the relative orientations of the inner disc, outer disc, and binary (Facchini et al. 2018; Zhu 2019). Discs with multiple breaks may have a complex series of shadowing features, as each disc shadows all of the discs external to it. However, Facchini et al. (2018) find that the flaring of the disc is an important geometrical feature for producing asymmetric shadowing when the inner and outer disc are at low relative angles. Since multiple disc breaking is less favored for flaring discs, the shadowing pattern may appear different. The local temperature changes caused by these shadows can generate spiral arms in the outer disc (Montesinos et al. 2016), so the thermal effects of these lanes may be important when attempting to reproduce observations.

Once a break is formed, it slowly drifts outwards over time. From the polar-aligning discs in Section 4.1, the drift rate is roughly $10^{-3}a_b/T_b$ for the inviscid simulations, and roughly twice as fast for the intermediate $\alpha = 10^{-2}$ simulation. For the break observed in the GW Orionis system, this translates to a drift rate of at least 7.7×10^{-4} au/yr. Assuming a constant outward drift rate, the break will reach the edge of the observed disc (500 au, Kraus et al. 2020) in roughly 6×10^5 years. This may be relatively short compared to the disc lifetime of 1-10 Myr (Andrews et al. 2009), and may imply that broken discs are transient features. On the other hand, the precession of the binary is constantly warping the disc, and should constantly generate breaks in the disc as long as it is still misaligned, similar to how other disc substructures such as gaps and spirals may be continuously generated by companions or orbiting planets. In this way, it may be possible for a disc to generate multiple breaks even though the disc conditions are only enough to satisfy a single break, as breaks move outward in the disc and new ones are generated at the breaking radius.

6 CONCLUSIONS

We have used grid-based hydrodynamic simulations to study the behavior of warped discs in the context of circumbinary discs created during early star formation. We find that the previously known behaviors for warped discs are reproduced well with the grid-based code, and that disc breaking is readily achieved for discs satisfying $\alpha \lesssim h/r$. From this we propose a viscous criterion for disc breaking, where the disc must undergo significant precession before aligning to the precession axis in order to break.

We also derive new formulations of the disc timescales in order to predict the location of a disc break. Our formulation for disc breaking suggests that breaking events are more likely when the disc is thinner, the inner cavity is smaller, and the disc power-law profiles are steeper. These criteria are well supported by our simulation results, and the predicted location for the breaking radius is in agreement with the breaks observed in our simulations. We also show that repeated disc breaking, predicted by our formulations, is possible.

When compared against our simulations, the analytic equations

produce breaking radii that are consistent with the observed locations. However, the sensitivity of these equations makes it difficult to use them in a predictive manner and precisely determine the location of the breaking radius. We have also applied our breaking formulation against the GW Orionis system to explain the discrepancies between previous simulations and their observed breaks, but better observational constraints are required to accurately assess whether the disc will break on its own. In the future, well-constrained disc parameters may be combined with our formulation to determine the breaking radii of warped discs.

ACKNOWLEDGEMENTS

This material is based upon work supported in part by the National Aeronautics and Space Administration under Grant No. 80NSSC20M0043 issued through the Nevada NASA Space Grant Consortium. Z. Z. acknowledges support from NASA award 80NSSC22K1413. Figures in this paper were made with the help of Matplotlib (Hunter 2007), NumPy (Harris et al. 2020), and VisIt (Childs et al. 2012). RGM and SHL acknowledge support from NASA through grants 80NSSC21K0395 and 80NSSC19K0443.

DATA AVAILABILITY

The data used in this paper is available upon request to the corresponding author.

REFERENCES

- Andrews S. M., Wilner D. J., Hughes A. M., Qi C., Dullemond C. P., 2009, *ApJ*, **700**, 1502
- Bae J., Hartmann L., Zhu Z., 2015, *ApJ*, **805**, 15
- Berger J. P., et al., 2011, *A&A*, **529**, L1
- Bi J., et al., 2020, *ApJ*, **895**, L18
- Burke B. F., 1957, *AJ*, **62**, 90
- Burrows C. J., Krist J. E., Stapelfeldt K. R., WFPC2 Investigation Definition Team 1995, in *American Astronomical Society Meeting Abstracts*. p. 32.05
- Casassus S., et al., 2015, *ApJ*, **811**, 92
- Childs H., et al., 2012, in *High Performance Visualization—Enabling Extreme-Scale Scientific Insight*. pp 357–372
- Debes J. H., et al., 2017, *ApJ*, **835**, 205
- Demianski M., Ivanov P. B., 1997, *A&A*, **324**, 829
- Doğan S., Nixon C. J., King A. R., Pringle J. E., 2018, *MNRAS*, **476**, 1519
- Dullemond C. P., Kimmig C. N., Zanazzi J. J., 2022, *MNRAS*, **511**, 2925
- Facchini S., Lodato G., Price D. J., 2013, *MNRAS*, **433**, 2142
- Facchini S., Juhász A., Lodato G., 2018, *MNRAS*, **473**, 4459
- Farago F., Laskar J., 2010, *MNRAS*, **401**, 1189
- Franchini A., Lubow S. H., Martin R. G., 2019, *ApJ*, **880**, L18
- Harris C. R., et al., 2020, *Nature*, **585**, 357
- Hunter J. D., 2007, *Computing in Science & Engineering*, **9**, 90
- Juhász A., Facchini S., 2017, *MNRAS*, **466**, 4053
- Katz J. I., 1973, *Nature Physical Science*, **246**, 87
- Kerr F. J., Hindman J. V., Carpenter M. S., 1957, *Nature*, **180**, 677
- King A. R., Livio M., Lubow S. H., Pringle J. E., 2013, *MNRAS*, **431**, 2655
- Kraus S., et al., 2020, *Science*, **369**, 1233
- Lepp S., Martin R. G., Lubow S. H., 2023, *ApJ*, **943**, L4
- Li H., Finn J. M., Lovelace R. V. E., Colgate S. A., 2000, *ApJ*, **533**, 1023
- Lodato G., Price D. J., 2010, *MNRAS*, **405**, 1212
- Lodato G., Pringle J. E., 2007, *MNRAS*, **381**, 1287
- Lovelace R. V. E., Li H., Colgate S. A., Nelson A. F., 1999, *ApJ*, **513**, 805
- Lubow S. H., Martin R. G., 2018, *MNRAS*, **473**, 3733
- Lubow S. H., Ogilvie G. I., 2000, *ApJ*, **538**, 326

- Lynden-Bell D., Pringle J. E., 1974, *MNRAS*, **168**, 603
- Marino S., Perez S., Casassus S., 2015, *ApJ*, **798**, L44
- Martin R. G., 2008, *MNRAS*, **387**, 830
- Martin R. G., Lubow S. H., 2017, *ApJ*, **835**, L28
- Martin R. G., Lubow S. H., 2018, *MNRAS*, **479**, 1297
- Martin R. G., et al., 2019, *ApJ*, **875**, 5
- Mathieu R. D., Adams F. C., Latham D. W., 1991, *AJ*, **101**, 2184
- Miyoshi M., Moran J., Herrnstein J., Greenhill L., Nakai N., Diamond P., Inoue M., 1995, *Nature*, **373**, 127
- Montesinos M., Perez S., Casassus S., Marino S., Cuadra J., Christiaens V., 2016, *ApJ*, **823**, L8
- Nealon R., Price D. J., Nixon C. J., 2015, *MNRAS*, **448**, 1526
- Nealon R., Ragusa E., Gerosa D., Rosotti G., Barbieri R., 2022, *MNRAS*, **509**, 5608
- Nixon C., King A., 2016, in Haardt F., Gorini V., Moschella U., Treves A., Colpi M., eds., Vol. 905, *Lecture Notes in Physics*, Berlin Springer Verlag. p. 45, doi:10.1007/978-3-319-19416-5_2
- Nixon C., King A., Price D., Frank J., 2012, *ApJ*, **757**, L24
- Nixon C., King A., Price D., 2013, *MNRAS*, **434**, 1946
- Ogilvie G. I., 1999, *MNRAS*, **304**, 557
- Papaloizou J. C. B., Lin D. N. C., 1995, *ApJ*, **438**, 841
- Papaloizou J. C. B., Pringle J. E., 1983, *MNRAS*, **202**, 1181
- Pettersson J. A., Rothschild R. E., Gruber D. E., 1991, *ApJ*, **378**, 696
- Pringle J. E., 1981, *ARA&A*, **19**, 137
- Pringle J. E., 1992, *MNRAS*, **258**, 811
- Rabago I., Zhu Z., Martin R. G., Lubow S. H., 2023, *MNRAS*,
- Raj A., Nixon C. J., Doğan S., 2021, *ApJ*, **909**, 81
- Scott D. M., Leahy D. A., Wilson R. B., 2000, *ApJ*, **539**, 392
- Shakura N. I., Sunyaev R. A., 1973, *A&A*, **500**, 33
- Shu F. H., Cuzzi J. N., Lissauer J. J., 1983, *Icarus*, **53**, 185
- Smallwood J. L., Lubow S. H., Franchini A., Martin R. G., 2019, *MNRAS*, **486**, 2919
- Smallwood J. L., Nealon R., Chen C., Martin R. G., Bi J., Dong R., Pinte C., 2021, *MNRAS*, **508**, 392
- Stone J. M., Tomida K., White C. J., Felker K. G., 2020, arXiv e-prints, p. arXiv:2005.06651
- Takeuchi T., Lin D. N. C., 2002, *ApJ*, **581**, 1344
- Young A. K., Stevenson S., Nixon C. J., Rice K., 2023, arXiv e-prints, p. arXiv:2306.11809
- Zanazzi J. J., Lai D., 2018, *MNRAS*, **473**, 603
- Zhu Z., 2019, *MNRAS*, **483**, 4221
- Zhu Z., Dong R., Stone J. M., Rafikov R. R., 2015, *ApJ*, **813**, 88

This paper has been typeset from a $\text{\TeX}/\text{\LaTeX}$ file prepared by the author.